PHYSICAL REVIEW APPLIED **22,** 014025 (2024)

Editors' Suggestion

Measurement of fractional charge in elastic plates with disclinations

Meng-Yang Liu,[1] Fei-Yang Sun,[2] Ze-Guo Chen,[3,*] Zhen Wang,[1,4,†] Ming-Hui Lu,[1,5,‡] and
Yan-Feng Chen[1,5]

[1] *National Laboratory of Solid State Microstructures & Department of Materials Science and Engineering, Nanjing University, Nanjing, Jiangsu 210093, China*
[2] *Key Laboratory of Modern Acoustics, MOE, Institute of Acoustics, School of Physics, Nanjing University, Nanjing, Jiangsu 210093, China*
[3] *School of Materials Science and Intelligent Engineering, Nanjing University, Suzhou 215163, China*
[4] *School of Electrical and Automation Engineering, Jiangsu Key Laboratory of 3D Printing Equipment and Manufacturing, Nanjing Normal University, Nanjing, China*
[5] *Jiangsu Key Laboratory of Artificial Functional Materials, Nanjing University, Nanjing, Jiangsu 210093, China*

(Received 12 March 2024; revised 31 May 2024; accepted 7 June 2024; published 11 July 2024)

In topological crystalline insulators, the presence of crystalline symmetries can lead to a filling anomaly—a mismatch in electron counts that causes quantized fractional charges at boundaries. These charges act as a critical probe of crystalline topology and are notably present even in electrically neutral systems, including artificial photonic and phononic systems. In these contexts, the boundary-localized fractional charges are represented by the local density of states, which is integrated over a specific frequency range (and is referred to as the integrated mode density). Here we report our measurement of the local density of states in an elastic wave lattice system. We propose an accurate approach to the measurement of the system's Green's function, achieved through piezoelectric transducer excitation and noncontact laser vibrometry detection. The experimental design includes both one-dimensional elastic plates and two-dimensional lattices with disclination defects. The experimental results conclusively show quantitative differentiation of these phases as well as the fractional charge, i.e., the fractional integrated mode density trapped in disclinations. Our approach provides valuable insights into the measurement of the local density of states in elastic systems, with implications for vibration enhancement and structural vibration control.

DOI: 10.1103/PhysRevApplied.22.014025

I. INTRODUCTION

Topological insulators (TIs) are materials that, despite having a band gap like ordinary insulators, exhibit conducting states at their edges or surfaces [1,2]. These edge states are protected by the topological characteristics of the material, and they give rise to behaviors not accounted for by conventional band theory. Topological crystalline insulators (TCIs), on the other hand, extend this concept by incorporating the symmetry of the crystal lattice into the topological framework [3]. While TIs rely on time-reversal symmetry for the protection of their surface states, TCIs derive their exotic surface properties from the crystal symmetry itself [3–6]. In contrast to the bulk-edge-correspondence-induced gapless edge states in the gap of TIs, such spectral features are often absent in TCIs. The protected observables in TCIs are quantized multipole moments (instead of common topological invariants in TIs) that manifest as lower-order moments bounded at boundaries [4,7]. When crystalline symmetries are present, some TCIs exhibit a filling anomaly, characterized by a discrepancy between the electron count in an energy band and the electron number needed to maintain charge neutrality [8,9]. This mismatch gives rise to quantized fractional charges at edges and even lower dimensional boundaries [10]. For instance, the presence of corner-localized charges, quantized in fractions of the electronic charge e, can occur as a result of a filling anomaly in C_n-symmetric crystalline insulators with zero polarization, specifically when corners are introduced. Such fractional corner charges, not directly related to corner-localized states, are powerful indices to distinguish different phases in certain symmetric TCIs. Furthermore, disclinations, defined as defects of rotation symmetry, are also expected to trap fractional charges [11,12]. Thus, the measurement of these charges serves as an efficient probe of the bulk topology [9,13–15].

---

[*] Contact author: zeguoc@nju.edu.cn
[†] Contact author: 61235@njnu.edu.cn
[‡] Contact author: luminghui@nju.edu.cn

An equivalent quantity of boundary-localized fractional charge is the integrated local density of states (LDOS), where the integrations are conducted over a given frequency range. The focus has shifted towards developing methods for the experimental measurement of the LDOS. In electronic systems, the LDOS at the Fermi level can be probed by scanning tunneling microscopy using tunneling current [16]. In microwave metamaterials, probing the radiation resistance of an inserted subwavelength antenna through a microwave network analyzer gives the LDOS [14,15,17]. Similar approaches are conducted in acoustics by measuring the emission rate of subwavelength monopole sources [18]. Accurately measuring the LDOS presents significant challenges. The primary difficulty lies in the discretization of the measured unit cells into many regions within the systems under consideration, which introduces errors. This is especially problematic in certain dielectric photonic crystal structures where only the electric field in the air can be conveniently measured. Additionally, contact measurements inherently disturb the state being measured, resulting in the detection of a perturbed state influenced by the presence of the probe.

In this study, we introduce an elastic wave lattice system, where the system eigenstates are represented by flexural displacements of discrete elastic plates [19–21]. In such an elastic system, the fractional mode charge can be expressed as the fractional integrated mode density (IMD). The Green's function of the system is extracted by exciting these eigenstates through the piezoelectric transducer on each plate and measuring the resultant responses. Noncontact laser vibrometry is employed to mitigate detector perturbations. As the LDOS is proportional to the imaginary part of the Green's function [22], the measurement for the density of states becomes feasible by measuring the Green's function across all plates.

Our experimental approach involves three sample sets. Initially, we verify our method using a one-dimensional (1D) elastic plate, corresponding to the nontrivial phase of the Su-Schrieffer-Heeger (SSH) model [23]. Subsequently, we construct two lattices with −90° Frank angle disclination defects in different C_4-symmetric lattices [11]. The experiments quantitatively differentiate these phases and confirm the robust trapping of fractional IMD by disclination defects. This model serves as a versatile platform for investigating fractional IMD in various disclinations, potentially advancing LDOS tailoring in elastic systems and applications in structural vibration control.

II. FRACTIONAL CHARGE

Compared with conventional TIs, TCIs exhibit additional crystalline symmetries, in which the filling anomaly may arise accompanied by fractional charges [8,9]. Taking the 1D SSH model with nine unit cells, for example, in the tight-binding model, only the nearest-neighbor coupling is considered. As shown in Fig. 1(a), the intracell (intercell) coupling is r (s). For neutrality of the whole model, each unit cell has a positive ion with charge $|e|$. As shown in Fig. 1(b), when $r > s$, the Wannier center, which represents the center-of-mass location of electrons, locates at the center of each unit cell and the system has charge neutrality. In comparison, when $r < s$, the Wannier center is located at the edge of each unit cell. Thus, there are eight or ten electrons due to reflection symmetry if we consider the

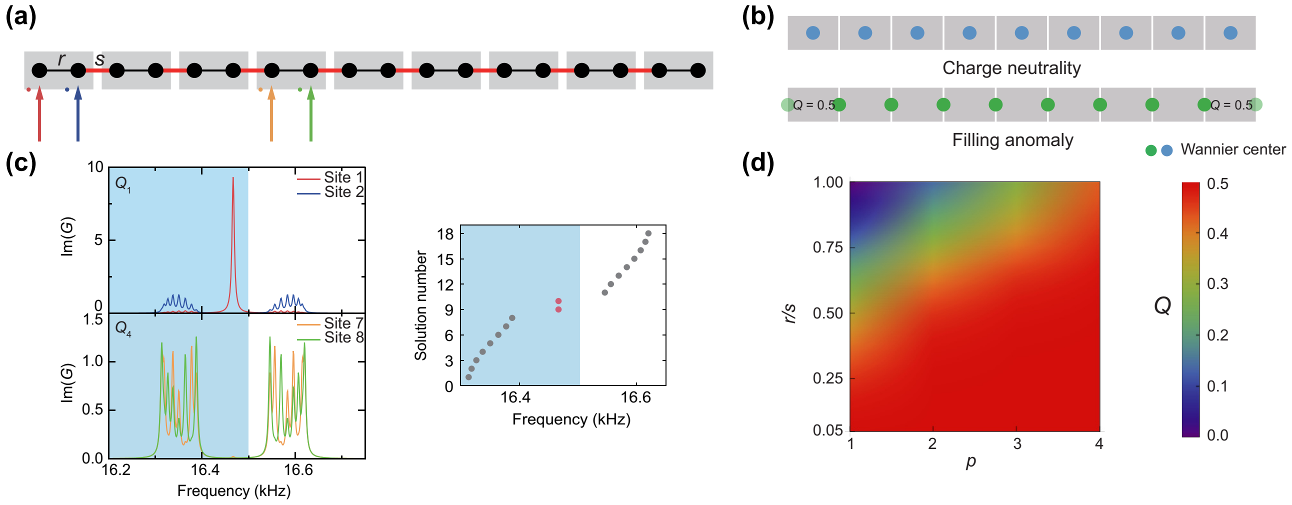

FIG. 1. The fractional charge in the one-dimensional (1D) Su-Schrieffer-Heeger (SSH) model. (a) The 1D SSH model with nine unit cells. The gray rectangles label the unit cells. The points (arrows) in different colors label sources (detectors). (b) The different positions of Wannier centers in charge-neutral (blue points) and filling-anomaly phases (green points). Solid (faded) points represent bulk (boundary) Wannier centers. (c) Imaginary part of different site responses simulated from the Green's function. (d) The fractional charge of the edge unit cell in (a), which is calculated up to the pth cell with a varied coupling ratio r/s.

Fermi level in the gap in which the filling anomaly arises. Consequently, an additional charge $Q = 0.5e$ is trapped at the edge. The mode charge Q_p, that is, the IMD at the pth unit cell, can be obtained in units of the electron charge e by integrating the LDOS $\rho(\omega)$ over a specific frequency and space domain as follows:

$$Q_p = \int_{\omega_1}^{\omega_2} d\omega\rho(\omega), \tag{1}$$

where the integration in real space is within the pth unit cell and the frequency range $\Delta\omega = \omega_2 - \omega_1$ covers all states below the Fermi level. The LDOS $\rho(\omega)$ is proportional to the imaginary part of Green's function $\overleftrightarrow{G}(\omega)$ at corresponding sites [22,24],

$$\overleftrightarrow{G}(\omega)_{m,n} = \sum_{j=1}^{N} \frac{|\tilde{\phi}_j^R\rangle\langle\tilde{\phi}_j^L|}{\omega - \tilde{\omega}_j + i\eta_j}(m,n), \tag{2}$$

where m (n) labels the source (detector) location and the matrix element $\overleftrightarrow{G}(\omega)_{m,n}$ corresponds to m rows and n columns of the Green's function. Meanwhile, the tensor part consists of the normalized biorthogonal right eigenstate $(|\tilde{\phi}_j^R\rangle)$ and left eigenstate $(\langle\tilde{\phi}_j^L|)$ of the Hamiltonian for the system with N states, and $\tilde{\omega}_j - i\eta_j$ is the eigenvalue corresponding to the loss coefficient η_j. Informally, the Green's function uncovers the response of the system under point-source excitation where the response of the mth site is defined as $\overleftrightarrow{G}(\omega)_{m,m}$. We plot the imaginary part of Eq. (2) as a function of the excitation frequency ω, as shown in the left panel of Fig. 1(c). Here, the on-site energy is set to 16 467 Hz and the intracell (r) and intercell (s) couplings are set to 40 and 115 Hz, respectively, extracted from the realistic model studied later. A sharp peak appears at the edge site response, indicating the existence of edge states in the gap. We integrate the responses of two unit cells ($p = 1$ and 4) as $Q_1 = \int_{\omega_1}^{\omega_2} \mathrm{Im}[G(\omega)_{1,1}] + \int_{\omega_1}^{\omega_2} \mathrm{Im}[G(\omega)_{2,2}]$ and $Q_4 = \int_{\omega_1}^{\omega_2} \mathrm{Im}[G(\omega)_{7,7}] + \int_{\omega_1}^{\omega_2} \mathrm{Im}[G(\omega)_{8,8}]$, respectively, where the integration regions are shaded blue in Fig. 1(c). The calculated normalized mode charge $Q = Q_1/Q_4 = 1.44$. At the limit that the intracell coupling r is adiabatically tuned to 0, the electrons are exactly localized at the Wannier centers and the result is exactly 1.5, indicating a fractional charge 0.5e at the edge unit cell. Considering a realistic model with finite size, as the ratio of r to s moves away from 0, the finite size effect delocalizes the edge states into bulk sites [25]. More edge sites (larger p) are required to capture the fractional charge 0.5e

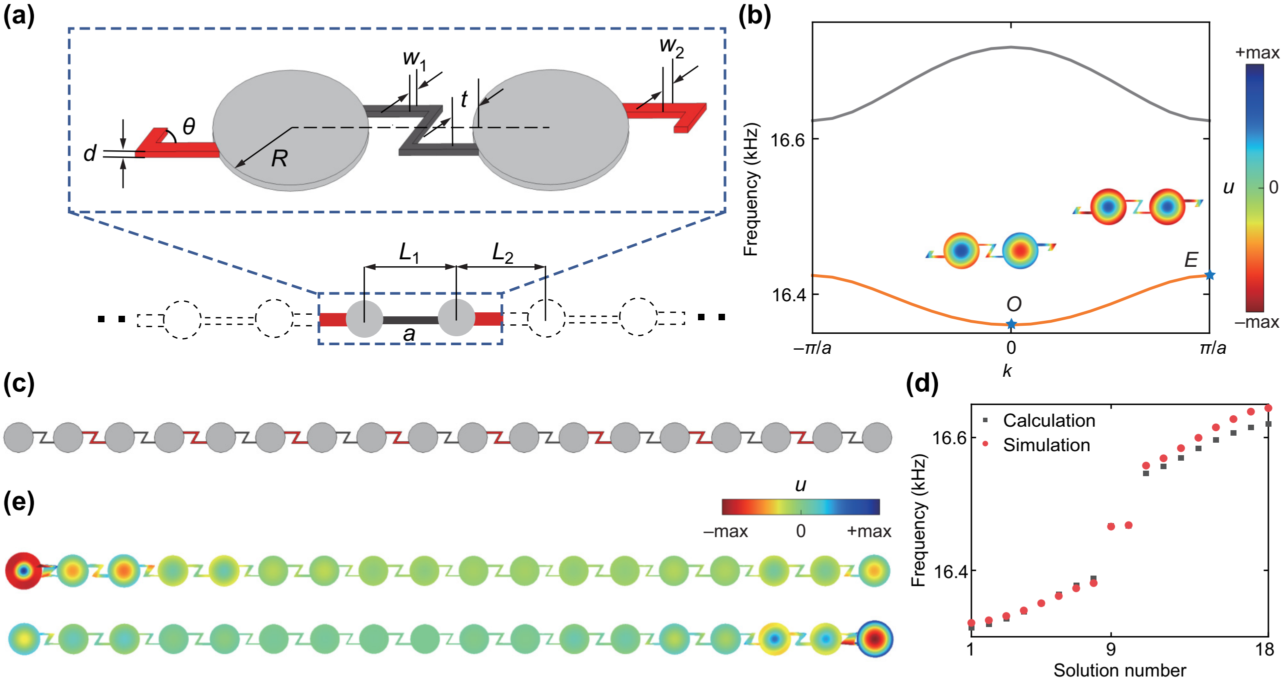

FIG. 2. The elastic 1D SSH model. (a) An elastic unit cell with adjustable parameters. The red and black lines label the strong and weak couplings. (b) The simulated bands of the 1D SSH model with periodic boundary conditions. The inset shows the eigenfunctions represented by the flexural displacement u. O and E stand for the parity at the $k = 0$ and $k = \pi/a$ points, odd and even, respectively. (c) The planform of the constructed elastic lattice for the finite-size 1D SSH model. (d) The simulated (red points) and calculated (black squares) spectra where in-gap edge states are plotted in (e).

in the calculation $Q = \left(\sum_p Q_p/Q_{\text{bulk}}\right) \bmod 1$ when r/s is close to the phase transition point $r/s = 1$, as shown in Fig. 1(d).

III. MEASUREMENTS

A. 1D SSH model

We design the lattice models using elastic plates [26–31] to experimentally measure the Green's function to verify the IMD. Corresponding to the theoretical Hamiltonian in Sec. II, only the lower-order vibration mode of the plates is considered [32]. Therefore, in order to reduce the disturbance of the couplings to the eigenfrequency of the plate, we employ a chiral-symmetric elastic steel unit cell with polygonal couplings. The material density is 7.762 g/cm^3, the Poisson's ratio and Young's modulus are 0.29 and 193 GPa, respectively. As depicted in Fig. 2(a), tunable plates and different polyline structures are constructed with a common thickness d to simulate the sites and their couplings, respectively [33]. The plates have a radius R of 15 mm, between which the connecting beams bend at the angle $\theta = 60^\circ$, deviating from the center line by the length $t = 5$ mm. In order to distinguish between different couplings and modify the band topology, the distance between plate centers (L_1, L_2) and the width of the beams (w_1, w_2) are adjusted within a reasonable range. Considering the 1D SSH model with periodic boundary conditions, we set $d = 1.75$ mm, $L_1 = 49.7$ mm, $L_2 = 50.6$ mm, $w_1 = 1.3$ mm, and $w_2 = 2.1$ mm so that the intracell coupling is weaker than the intercell one. Since our system is captured by the lattice model in elastic plates, the flexural displacement u represents the eigenfunction. As shown in Fig. 2(b), in the simulation for the unit cell with length $a = L_1 + L_2$, there is a parity inversion in the first band between point O and point E in the Brillouin zone, which showcase odd parity and even parity, respectively. With the same structural parameters as the finite-size 1D SSH model mentioned in Fig. 1, the elastic lattice is constructed as shown in Fig. 2(c). Its simulated and calculated energy bands are given in Fig. 2(d), from which we can find two edge states emerging in the band

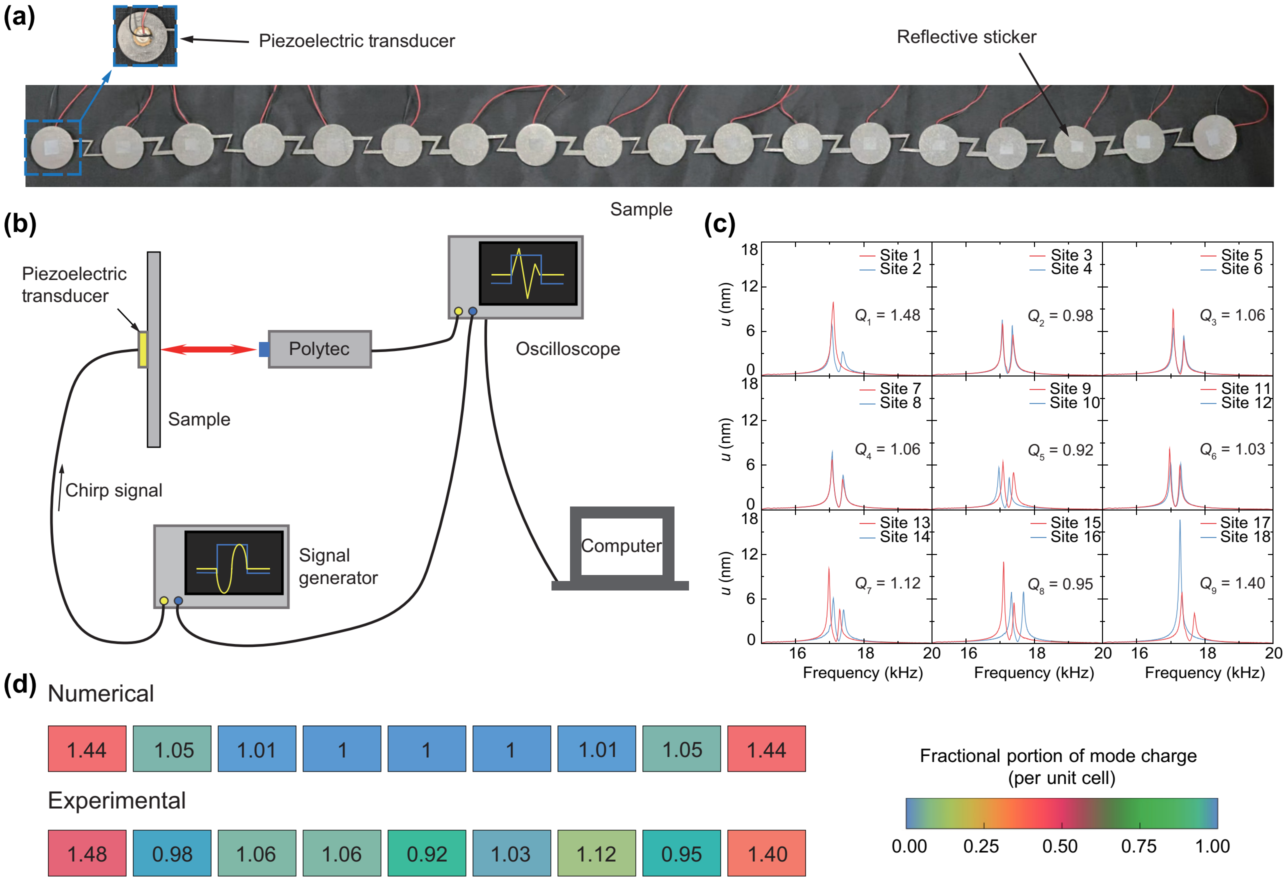

Numerical

1.44	1.05	1.01	1	1	1	1.01	1.05	1.44

Experimental

1.48	0.98	1.06	1.06	0.92	1.03	1.12	0.95	1.40

FIG. 3. Fractional integrated mode density (IMD) in 1D elastic plates. (a) The 1D SSH sample with piezoelectric transducers and reflective stickers affixed to it. (b) The experimental setup. (c) Measured site responses and the normalized IMDs for all the unit cells. Red and blue curves label the displacement responses for different sites in each unit cell. (d) The numerical and experimental IMDs within each unit cell of the 1D SSH model.

gap. Figure 2(e) shows the simulated eigenfunctions for the in-gap edge states, which localize at both ends of the model.

We utilize the Purcell effect, which associates the site response $u(\omega)_{j,j}$ with the source emission $\mathrm{Im}[G(\omega)_{j,j}]$ as well as the LDOS [18,34,35]. The imaginary part of the Green's function defined in our system, resulting from a point-source excitation with a constant source strength attached at each site, is captured by measuring the site displacement u under the corresponding site excitation. In our experimental setup, we affix piezoelectric transducers and reflective stickers to both sides of each plate in the sample [Fig. 3(a)], which is suspended in a suitable position and guaranteed to be free from vertical external interference. A chirp signal drives the piezoelectric transducer behind the target plate, allowing precise measurement of displacement signals using a Polytec OFV-055 laser vibrometer focused on the reflective sticker [Fig. 3(b)]. By performing a Fourier transform on these displacement signals into the frequency domain, we plot the site responses for all sites and label the normalized IMD for each unit cell, as shown in Fig. 3(c). We compare the experimental results with the numerical results in Fig. 3(d). Note that the IMDs at the two boundaries in the experiment are not equal. This discrepancy may be attributed to machining errors and the inconsistency in the emission spectra among different piezoelectric elements. Nevertheless, our results still demonstrate the efficacy of employing a noncontact measurement approach to measure the fractional IMD in the elastic lattice model.

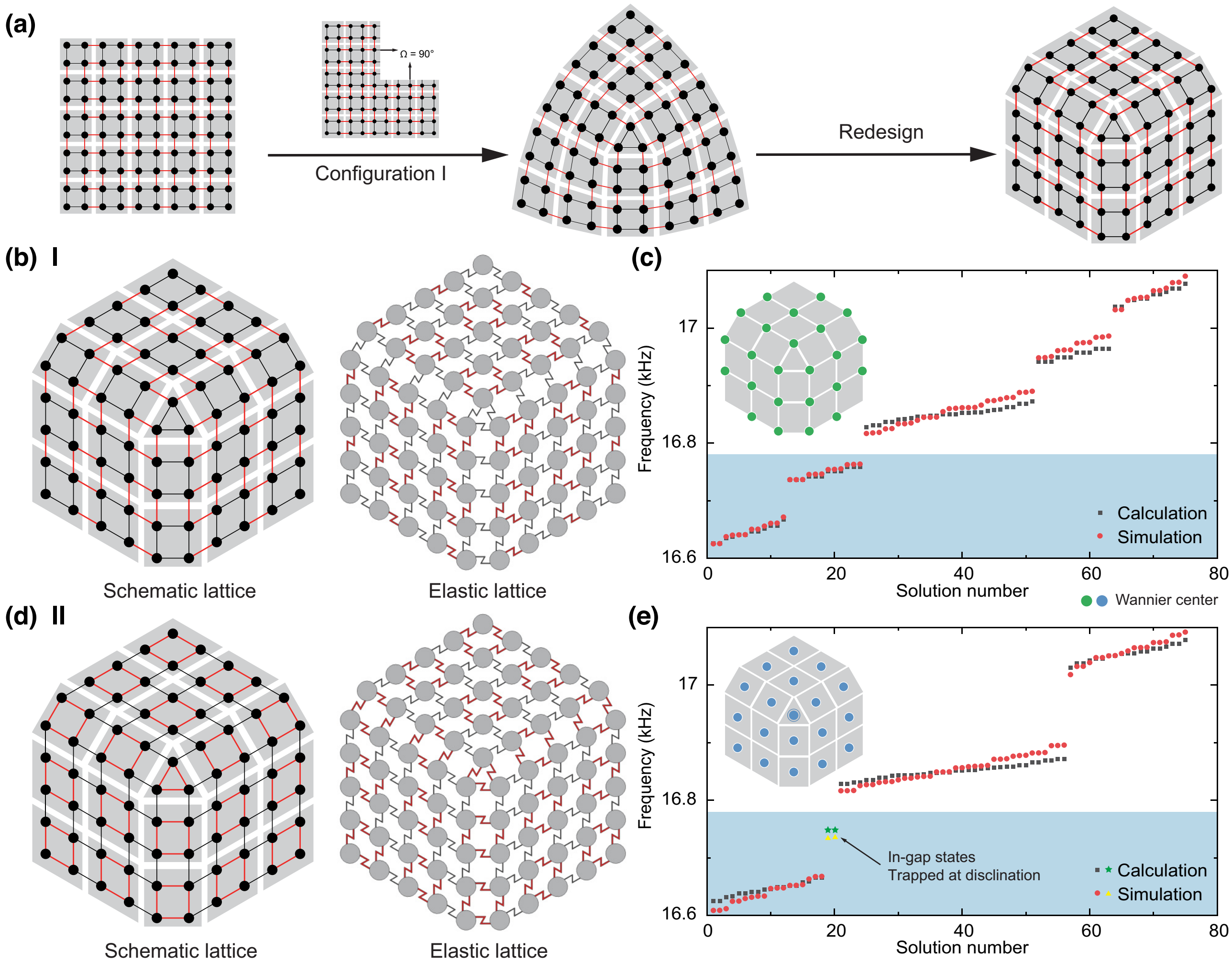

FIG. 4. Two-dimensional (2D) elastic plates with disclinations. In (a),(b),(d), the black points label the lattice sites and the gray areas label the unit cells. Red and black lines connecting the points label the strong and weak couplings, respectively. (a) Deformation from $N \times N$ unit cells where $N = 5$ is an odd number. (b),(d) The schematic lattices and the elastic lattices for configuration I and configuration II, respectively. (c),(e) The simulated (red points and yellow triangles) and calculated (black squares and green stars) energy bands for configuration I and configuration II, respectively. The Wannier centers of configuration I (II) in the context of unit cells (gray areas) are labeled by green (blue) points. In (e), the highlighted states are localized at the disclination and contribute a charge of 2 to the central cell, corresponding to the central Wannier center with a circle.

B. Two-dimensional disclination model

Disclination, a prevalent defect in crystalline solids, has been demonstrated to effectively trap fractional charges at the core and is expected to serve as a robust bulk probe for various topological crystalline phases [8,11,13,14,36–38]. As depicted in Fig. 4(a), a disclination can be constructed by removing a 90° sector from the lattice's central unit and reattaching the remaining parts together [13]. We illustrate this concept using configuration I where red (black) lines indicate weak (strong) couplings, respectively. Conversely, for the construction of configuration II, these couplings are interchanged. Moreover, to facilitate the design as shown in Fig. 4(a), we rearrange the sites to keep uniform lengths corresponding to identical strong (weak) couplings, otherwise the connecting beams would perturb the effective on-site energy [39].

Figures 4(b) and 4(d) show the schematic lattices and the corresponding planform of elastic lattices for configurations I and II, respectively. The construction parameters

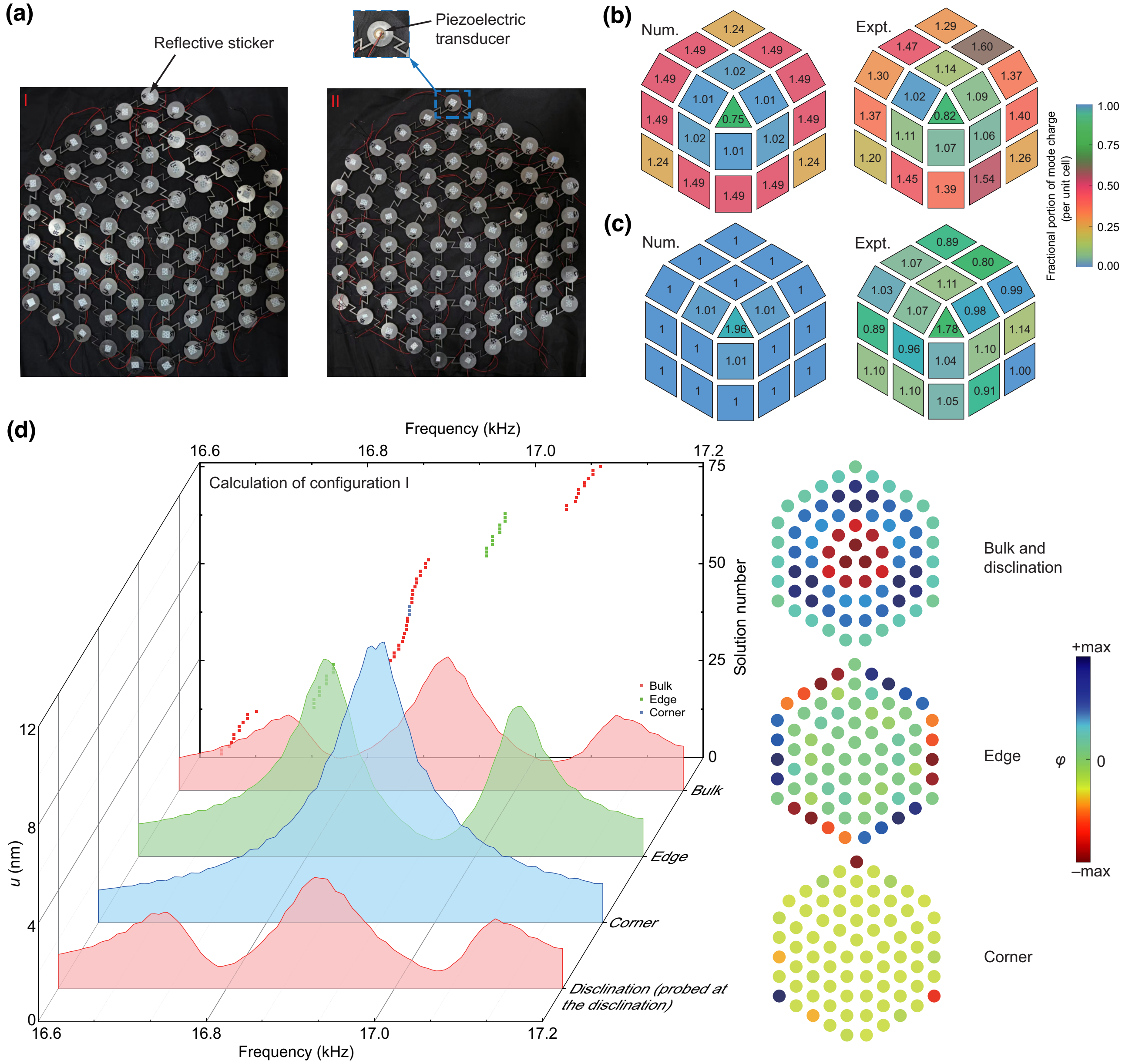

FIG. 5. Fractional IMD trapped in disclinations of 2D elastic plates. (a) The samples for both configurations with piezoelectric transducers and reflective stickers. (b),(c) The numerical and experimental IMDs within each unit cell for configuration I (b) and II (c). (d) The measured site responses and the calculated spectra of configuration I. For the energy bands in the background, red, green, and blue squares label the bulk, edge, and corner states, respectively, corresponding to the spectrum in the same color. Three inset eigenmodes represent the bulk and disclination, edge, and corner states, respectively.

are as follows: the thickness d is set to be 1.80 mm, the bond lengths L and the widths w of the beams for strong and weak couplings are set to $L_s = 50.8$ mm, $w_s = 2$ mm, $L_w = 50$ mm, and $w_w = 1.1$ mm, respectively. In Figs. 4(c) and 4(e), we plot simulated eigenspectra, which both exhibit good agreement with theoretical calculations used as references. Taking the same Fermi level, as shown by the blue shaded areas in Figs. 4(c) and 4(e), the lowest two bands are occupied in both configurations. In configuration I, Wannier centers are located at the unit cell corners [Fig. 4(c)]. Thus, in an ideal case, the center cell with the disclination traps a mode charge of $3/4$, while the edge unit cells possess a charge of $3/2$ and the corner unit cells have a charge of $5/4$. Conversely, in configuration II, the Wannier center is located at the center of each unit cell [Fig. 4(e)]. As a result, no fractional charges exist within this configuration [13]. However, in configuration II, we observe the presence of two localized bound states within the disclination, resulting in a charge contribution of 2 to the central cell [as depicted in Fig. 4(e)]. Consequently, there is a charge of 2 within the disclination and a charge of 1 within each of the other unit cells. Such in-gap states appear naturally in configuration II. To facilitate comprehension, we consider the thermodynamic limit with $w_w = 0$: three atoms connected by identical couplings with the disregarded potential energy. For this model, the tight-binding Hamiltonian can be expressed as

$$H = \begin{pmatrix} 0 & t & t \\ t & 0 & t \\ t & t & 0 \end{pmatrix},$$

where t represents the coupling strength. Consequently, one eigenstate with eigenvalue $2t$ and two eigenstates with eigenvalues $-t$ can be obtained, corresponding to the two bound states within the energy gap depicted in Fig. 4(e). This localization enables these states to be more closely linked to the bulk characteristics of the model and potentially find applications in laser development.

We affix both piezoelectric transducers and reflective stickers to the surfaces of all plates in both configurations [Fig. 5(a)]. As explained before, in unit p for both configurations the mode density Q_p can be obtained by adding up the ith response $\mathrm{Im}[G(\omega)_{i,i}]$ in the spatial and frequency domain as follows:

$$Q_p = \sum_{i}^{\mathrm{unit}\,p} \int_{\omega_1}^{\omega_2} \mathrm{Im}[G(\omega)_{i,i}], \tag{3}$$

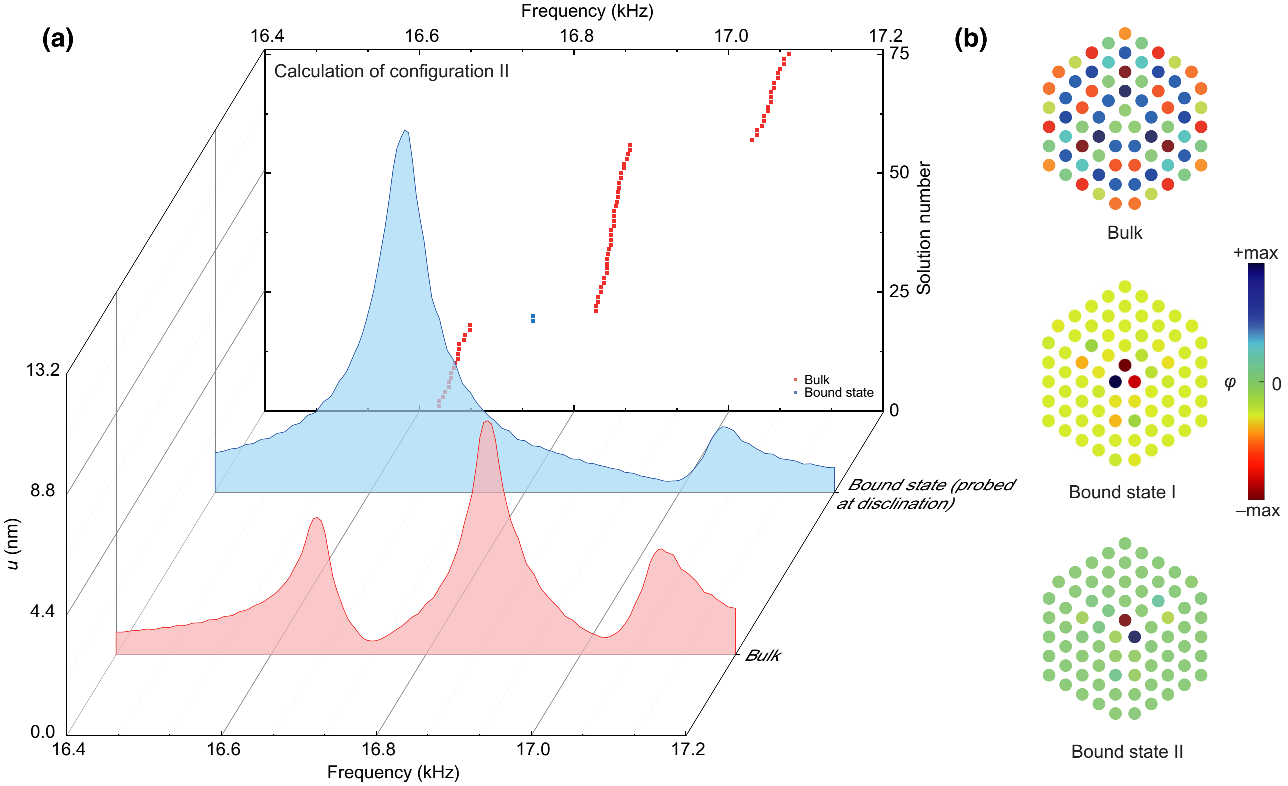

FIG. 6. Trapped in-gap states at the disclination of configuration II. (a) The measured site responses and the calculated spectra of configuration II. For the calculated spectra in the background, red and blue squares label the bulk and bound states localized at the disclination, respectively, corresponding to the spectrum in the same color. (b) Three eigenmodes represent the bulk state and two bound states localized at the disclination, respectively.

where ω_1 and ω_2 label the upper and lower limits of the integral, respectively. Color block diagrams in Figs. 5(b) and 5(c) illustrate the numerical results as well as experimental results for these two configurations, respectively. Obviously, we can clearly distinguish these two configurations through the distribution of the IMD. Moreover, the fractional IMD trapped at the disclination can be observed, which is consistent with the predictions [11,13].

Measured displacement spectra for configurations I and II are depicted in Figs. 5(d) and 6, respectively, consistent with the energy bands displayed in the background. Note that in configuration I, no localized state exists at disclination. The spectrum probed at the disclination is similar to that at the bulk, as also predicted by the theoretically calculated eigenmodes on the right side of Fig. 5(d). Nevertheless, the calculated IMD still shows fractional behavior that implies the nontrivial bulk topology. Therefore, in addition to the observed edge and corner responses, the fractional IMDs at boundaries and disclinations can also probe the bulk topology. In comparison, we can observe localized states trapped at the disclination in configuration II. This localization mechanism enables these states to lie deep within the bulk away from the material boundary. Applications for lasers are anticipated since the state is surrounded by bulk insulators without radiative decay.

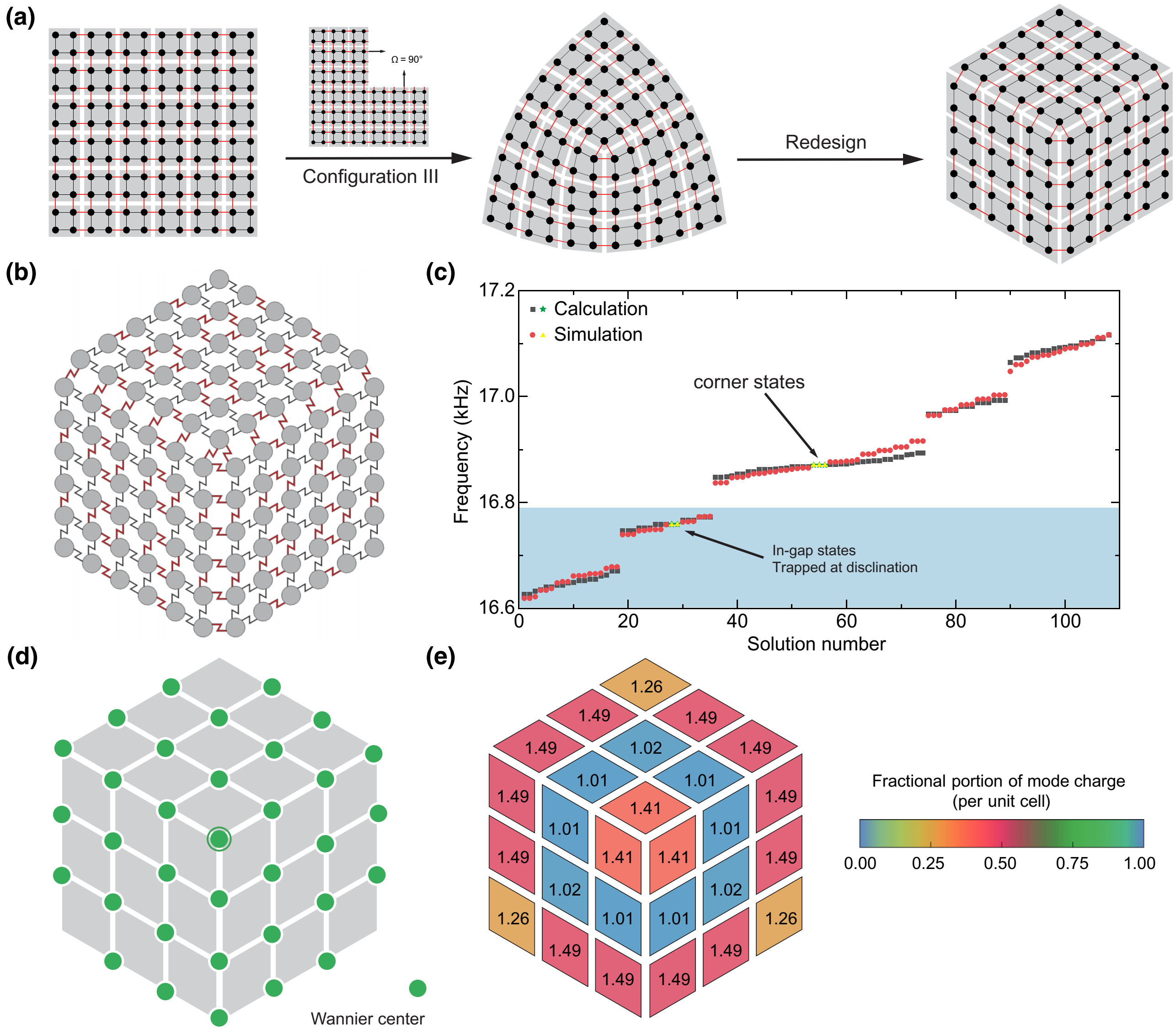

FIG. 7. An alternative disclination phase. (a) Deformation from $N \times N$ unit cells where $N = 6$ is an even number. (b) The constructed elastic lattice for configuration III. (c) The simulated (red points and yellow triangles) and calculated (black squares and green stars) energy bands for configuration III. We highlight the disclination bound states and the corner states. (d) The Wannier centers (green points) of configuration III in the context of unit cells (gray areas). The central green point with a circle highlights the central Wannier center contributing the charge of 2. (e) The calculated charge distribution for configuration III.

IV. OUTLOOK

For configuration I mentioned previously, the disclination center is situated inside the central cell, which results from the initial lattice with an odd number of unit cells on one side. However, considering the initial lattice with an even number of unit cells on one side, the disclination center is located at the junction of the central cells. As a result, an alternative disclination structure, configuration III, can be constructed as depicted in Fig. 7(a). Similar to the aforementioned configurations, configuration III is also redesigned and constructed within the elastic lattice [Fig. 7(b)]. The construction parameters are slightly adjusted as follows: the thickness d is set to be 1.80 mm, and the bond lengths L and widths w of the beams for strong and weak couplings are set to $L_s = 50.5$ mm, $w_s = 2.1$ mm, $L_w = 50$ mm, and $w_w = 1.1$ mm, respectively.

The simulated energy bands also exhibit good agreement with the theoretical calculation [Fig. 7(c)]. We label the Wannier centers in Fig. 7(d). Ideally, most Wannier centers contribute a charge of 1 and divide evenly among their adjacent unit cells, while the central Wannier center contributes a total charge of 2 resulting from the two localized bound states within the disclination, as shown in Fig. 7(c). Consequently, in configuration III, besides the mode charge of 1 for the bulk region, 3/2 in the edges, and 5/4 at the corners, each disclination unit cell acquires a mode charge of $3/4 + 2/3 = 17/12 \approx 1.42$. Considering the realistic couplings as well as the finite size effect in our lattice model, the calculated charge distribution according to Eq. (3) is shown in Fig. 7(e).

In terms of both state characteristics and the charge distribution, configuration III appears to amalgamate the features of configurations I and II. This can be elucidated by its lattice attributes: configuration III incorporates both the sequence of coupling strengths at the boundary of configuration I and the strong couplings surrounding the disclination at the center of configuration II. In other words, configuration III reproduces the boundary in configuration I and the disclination in configuration II. Considering the existence of in-gap edge states in configuration I and in-gap disclination states in configuration II, configuration III provides a mechanism for bound states in the edge continuum [40–42] as shown in Fig. 7(c).

V. CONCLUSIONS

In this study, we design several elastic lattice models to experimentally observe the fractional IMDs at edges, corners, and disclination defects. Unlike the previous approach of full-field scanning to measure the LDOS, the elastic lattice system we introduce requires the measurement of the displacement at only a single point. Additionally, the measurement errors are further reduced through noncontact laser vibrometry. Moreover, disclination bound states in the edge state continuum with atypical charge distributions are explored. Our experiments confirm the feasibility of probing bulk topology through the measurement of the LDOS. Our approaches are promising to serve as a robust elastic platform for exploring other topological phases with disorder introduced, ultimately contributing to advancements in topological phononics.

ACKNOWLEDGMENTS

This work is supported by the National Key Research and Development Program of China (Grants No. 2023YFA1406900 and No. 2023YFA1407700), the development project of the Ministry of Science and Technology (Grant No. 2022YFA1404404), the National Natural Science Foundation of China (Grants No. 52027803 and No. 52394162) and 2022 Research Project on Basic Sciences (Natural Sciences) in Higher Education Institutions of Jiangsu Province (Grant No. 22KJB430031).

[1] M. Z. Hasan and C. L. Kane, Colloquium: Topological insulators, Rev. Mod. Phys. **82**, 3045 (2010).

[2] X.-L. Qi and S.-C. Zhang, Topological insulators and superconductors, Rev. Mod. Phys. **83**, 1057 (2011).

[3] L. Fu, Topological crystalline insulators, Phys. Rev. Lett. **106**, 106802 (2011).

[4] W. A. Benalcazar, B. A. Bernevig, and T. L. Hughes, Quantized electric multipole insulators, Science **357**, 61 (2017).

[5] W. A. Benalcazar, B. A. Bernevig, and T. L. Hughes, Electric multipole moments, topological multipole moment pumping, and chiral hinge states in crystalline insulators, Phys. Rev. B **96**, 245115 (2017).

[6] S. Liu, A. Vishwanath, and E. Khalaf, Shift insulators: Rotation-protected two-dimensional topological crystalline insulators, Phys. Rev. X **9**, 031003 (2019).

[7] C. W. Peterson, W. A. Benalcazar, T. L. Hughes, and G. Bahl, A quantized microwave quadrupole insulator with topologically protected corner states, Nature **555**, 346 (2018).

[8] W. A. Benalcazar, T. Li, and T. L. Hughes, Quantization of fractional corner charge in C_n-symmetric higher-order topological crystalline insulators, Phys. Rev. B **99**, 245151 (2019).

[9] C. W. Peterson, T. Li, W. A. Benalcazar, T. L. Hughes, and G. Bahl, A fractional corner anomaly reveals higher-order topology, Science **368**, 1114 (2020).

[10] B. Xie, H.-X. Wang, X. Zhang, P. Zhan, J.-H. Jiang, M. Lu, and Y. Chen, Higher-order band topology, Nat. Rev. Phys. **3**, 520 (2021).

[11] T. Li, P. Zhu, W. A. Benalcazar, and T. L. Hughes, Fractional disclination charge in two-dimensional C_n-symmetric topological crystalline insulators, Phys. Rev. B **101**, 115115 (2020).

[12] Z.-K. Lin, Q. Wang, Y. Liu, H. Xue, B. Zhang, Y. Chong, and J.-H. Jiang, Topological phenomena at defects in acoustic, photonic and solid-state lattices, Nat. Rev. Phys. **5**, 483 (2023).

[13] C. W. Peterson, T. Li, W. Jiang, T. L. Hughes, and G. Bahl, Trapped fractional charges at bulk defects in topological insulators, Nature **589**, 376 (2021).

[14] Y. Liu, S. Leung, F.-F. Li, Z.-K. Lin, X. Tao, Y. Poo, and J.-H. Jiang, Bulk–disclination correspondence in topological crystalline insulators, Nature **589**, 381 (2021).

[15] B. Xie, R. Huang, S. Jia, Z. Lin, J. Hu, Y. Jiang, S. Ma, P. Zhan, M. Lu, Z. Wang, Y. Chen, and S. Zhang, Bulk-local-density-of-state correspondence in topological insulators, Nat. Commun. **14**, 7347 (2023).

[16] J. Tersoff and D. R. Hamann, Theory of the scanning tunneling microscope, Phys. Rev. B **31**, 805 (1985).

[17] C.-P. Liang, Y. Liu, F.-F. Li, S.-W. Leung, Y. Poo, and J.-H. Jiang, Fractional topological numbers at photonic edges and corners, Phys. Rev. Appl. **20**, 034028 (2023).

[18] H. Ge, Z.-W. Long, X.-Y. Xu, J.-G. Hua, Y. Liu, B.-Y. Xie, J.-H. Jiang, M.-H. Lu, and Y.-F. Chen, Direct measurement of acoustic spectral density and fractional topological charge, Phys. Rev. Appl. **19**, 034073 (2023).

[19] G. Ma, M. Xiao, and C. T. Chan, Topological phases in acoustic and mechanical systems, Nat. Rev. Phys. **1**, 281 (2019).

[20] H. Xue, Y. Yang, and B. Zhang, Topological acoustics, Nat. Rev. Mater. **7**, 974 (2022).

[21] M. Oudich, N. J. Gerard, Y. Deng, and Y. Jing, Tailoring structure-borne sound through bandgap engineering in phononic crystals and metamaterials: A comprehensive review, Adv. Funct. Mater. **33**, 2206309 (2023).

[22] P. Sheng, *Introduction to Wave Scattering, Localization, and Mesoscopic Phenomena* (Springer, New York, 2006).

[23] W. P. Su, J. R. Schrieffer, and A. J. Heeger, Solitons in polyacetylene, Phys. Rev. Lett. **42**, 1698 (1979).

[24] K. Ding, G. Ma, M. Xiao, Z. Q. Zhang, and C. T. Chan, Emergence, coalescence, and topological properties of multiple exceptional points and their experimental realization, Phys. Rev. X **6**, 021007 (2016).

[25] B. Zhou, H.-Z. Lu, R.-L. Chu, S.-Q. Shen, and Q. Niu, Finite size effects on helical edge states in a quantum spin-Hall system, Phys. Rev. Lett. **101**, 246807 (2008).

[26] M. Serra-Garcia, V. Peri, R. Süsstrunk, O. R. Bilal, T. Larsen, L. G. Villanueva, and S. D. Huber, Observation of a phononic quadrupole topological insulator, Nature **555**, 342 (2018).

[27] X. Yan, R. Zhu, G. Huang, and F.-G. Yuan, Focusing guided waves using surface bonded elastic metamaterials, Appl. Phys. Lett. **103**, 121901 (2013).

[28] Y. Chen, G. Hu, and G. Huang, A hybrid elastic metamaterial with negative mass density and tunable bending stiffness, J. Mech. Phys. Solids **105**, 179 (2017).

[29] Y. Wang, B. Yousefzadeh, H. Chen, H. Nassar, G. Huang, and C. Daraio, Observation of nonreciprocal wave propagation in a dynamic phononic lattice, Phys. Rev. Lett. **121**, 194301 (2018).

[30] E. Riva, M. I. N. Rosa, and M. Ruzzene, Edge states and topological pumping in stiffness-modulated elastic plates, Phys. Rev. B **101**, 094307 (2020).

[31] Y. Xia, E. Riva, M. I. N. Rosa, G. Cazzulani, A. Erturk, F. Braghin, and M. Ruzzene, Experimental observation of temporal pumping in electromechanical waveguides, Phys. Rev. Lett. **126**, 095501 (2021).

[32] M. Miniaci, F. Allein, and R. K. Pal, Spectral flow of a localized mode in elastic media, Phys. Rev. Appl. **20**, 064018 (2023).

[33] W. Wang, Z.-G. Chen, and G. Ma, Synthetic three-dimensional $Z \times Z_2$ topological insulator in an elastic metacrystal, Phys. Rev. Lett. **127**, 214302 (2021).

[34] E. M. Purcell, H. C. Torrey, and R. V. Pound, Resonance absorption by nuclear magnetic moments in a solid, Phys. Rev. **69**, 37 (1946).

[35] M. Landi, J. Zhao, W. E. Prather, Y. Wu, and L. Zhang, Acoustic Purcell effect for enhanced emission, Phys. Rev. Lett. **120**, 114301 (2018).

[36] A. Rüegg and C. Lin, Bound states of conical singularities in graphene-based topological insulators, Phys. Rev. Lett. **110**, 046401 (2013).

[37] J. C. Y. Teo and T. L. Hughes, Existence of Majorana-fermion bound states on disclinations and the classification of topological crystalline superconductors in two dimensions, Phys. Rev. Lett. **111**, 047006 (2013).

[38] Y. Deng, W. A. Benalcazar, Z.-G. Chen, M. Oudich, G. Ma, and Y. Jing, Observation of degenerate zero-energy topological states at disclinations in an acoustic lattice, Phys. Rev. Lett. **128**, 174301 (2022).

[39] Z.-G. Chen, L. Wang, G. Zhang, and G. Ma, Chiral symmetry breaking of tight-binding models in coupled acoustic-cavity systems, Phys. Rev. Appl. **14**, 024023 (2020).

[40] C. W. Hsu, B. Zhen, A. D. Stone, J. D. Joannopoulos, and M. Soljačić, Bound states in the continuum, Nat. Rev. Mater. **1**, 16048 (2016).

[41] Z.-G. Chen, C. Xu, R. Al Jahdali, J. Mei, and Y. Wu, Corner states in a second-order acoustic topological insulator as bound states in the continuum, Phys. Rev. B **100**, 075120 (2019).

[42] L. Liu, T. Li, Q. Zhang, M. Xiao, and C. Qiu, Universal mirror-stacking approach for constructing topological bound states in the continuum, Phys. Rev. Lett. **130**, 106301 (2023).